

Boundary scheme for lattice Boltzmann modeling of microscale gas flow in organic-rich pores considering surface diffusion

Hong Zuo(左鸿), Shou-Chun Deng(邓守春), Hai-Bo Li(李海波)

Citation: Chin. Phys. B . 2019, 28(3): 030202. **doi:** 10.1088/1674-1056/28/3/030202
Journal homepage: http://cpb.iphy.ac.cn; http://iopscience.iop.org/cpb

What follows is a list of articles you may be interested in

A local energy-preserving scheme for Zakharov system

Qi Hong(洪旗), Jia-ling Wang(汪佳玲), Yu-Shun Wang(王雨顺)

Chin. Phys. B . 2018, 27(2): 020202. **doi:** 10.1088/1674-1056/27/2/020202

Local structure-preserving methods for the generalized Rosenau-RLW-KdV equation with power law nonlinearity

Jia-Xiang Cai(蔡加祥), Qi Hong(洪旗), Bin Yang(杨斌)

Chin. Phys. B . 2017, 26(10): 100202. **doi:** 10.1088/1674-1056/26/10/100202

Topology optimization using the improved element-free Galerkin method for elasticity

Yi Wu(吴意), Yong-Qi Ma(马永其), Wei Feng(冯伟), Yu-Min Cheng(程玉民)

Chin. Phys. B . 2017, 26(8): 080203. **doi:** 10.1088/1674-1056/26/8/080203

Consecutive induction melting of nickel-based superalloy in electrode induction gas atomization

Shan Feng(峰山), Min Xia(夏敏), Chang-Chun Ge(葛昌纯)

Chin. Phys. B . 2017, 26(6): 060201. **doi:** 10.1088/1674-1056/26/6/060201

Numerical analysis of a dual-pass pumping laser with weak absorption

Guang-Ju Zhang(张光举), Ma-Li Gong(巩马理), Wen-Qi Zhang(张文启)

Chin. Phys. B . 2017, 26(5): 050203. **doi:** 10.1088/1674-1056/26/5/050203

Boundary scheme for lattice Boltzmann modeling of micro-scale gas flow in organic-rich pores considering surface diffusion*

Hong Zuo(左鸿)[1,2], Shou-Chun Deng(邓守春)[1,†], and Hai-Bo Li(李海波)[1]

[1] State Key Laboratory of Geomechanics and Geotechnical Engineering, Institute of Rock and Soil Mechanics, Chinese Academy of Sciences, Wuhan 430071, China

[2] University of Chinese Academy of Sciences, Beijing 100049, China

(Received 16 August 2018; revised manuscript received 3 January 2019; published online 28 January 2019)

We propose a boundary scheme for addressing multi-mechanism flow in a porous medium in slip and early transition flow regimes, which is frequently encountered in shale gas reservoirs. Micro-gaseous flow in organic-rich shale involves a complex flow mechanism. A self-developed boundary scheme that combines the non-equilibrium extrapolation scheme and the combined diffusive reflection and bounce-back scheme (half-way DBB) to embed the Langmuir slip boundary into the single-relaxation-time lattice Boltzmann method (SRT-LBM) enables us to describe this process, namely, the coupling effect of micro-gaseous flow and surface diffusion in organic-rich nanoscale pores. The present LBM model comes with the careful consideration of the local Knudsen number, local pressure gradient, viscosity correction model, and regularization procedure to account for the rarefied gas flows in irregular pores. Its validity and accuracy are verified by several benchmarking cases, and the calculated results by this boundary scheme accord well with our analytical solutions. This boundary scheme shows a higher accuracy than the existing studies. Additionally, a subiteration strategy is presented to tackle the coupled micro-gaseous flow and surface diffusion, which necessitates the iteration process matching of these two mechanisms. The multi-mechanism flow in the self-developed irregular pores is also numerically investigated and analyzed over a wide range of parameters. The results indicate that the present model can effectively capture the coupling effect of micro-gaseous flow and surface diffusion in a tree-like porous medium.

Keywords: lattice Boltzmann method (LBM), surface diffusion, Langmuir slip model, boundary scheme

PACS: 02.60.Cb, 05.20.Dd, 02.60.Cb **DOI:** 10.1088/1674-1056/28/3/030202

1. Introduction

The accurate understanding of the fundamental flow mechanism of methane gas in complex micro/nanopores is crucial to the effective exploitation of unconventional reservoirs, the strata of which is associated with kerogen networks and organic matter. The unconventional reservoirs, such as shale reservoirs and other tight sandstone gas reservoirs, contain abundant micro-scale and nanoscale pores, the sizes of which vary in a wide range on a micro-scale from 2 nm up to 100 nm,[1] typically presenting multi-scale networks of pores. The non-Darcy flow, such as slip flow and early transition flow,[2] dominates in these multi-scale pore networks. In kerogen-rich pores, the coupled micro-scale effects and surface diffusion (induced by methane adsorption/desorption process) control the gas flows, involving a complex flow mechanism, while only the micro-gaseous flow exists in these inorganic pores in the absence of adsorption/desorption.

Despite its attracting significant research attention in recent years, the accurate flow mechanism of micro-gas in an organic-rich porous medium still has not been well addressed, because the existing models and parameters are geometry-dependent and not applicable to these irregular pores. Most of the current analytical models for micro-gaseous flow in organic/inorganic pores are limited to cases with simple geometries, such as tube and channel,[3–5] which are of limited applicability to shale reservoirs where complex irregular nanopores are ubiquitous. To our best knowledge, the multi-mechanism flow is still less understood, although some hypothetical models have been proposed to capture gas transport in organic nanopores considering surface diffusion.[3,4] Additionally, the experiment-based studies are less accurate due to the extremely low mass transport capability of shale and difficulty in controlling laboratory conditions.[6–9]

As a replacement or supplementary to experiments and theories, numerical simulation has become a promising and effective tool to research and reveal some micro-scale physical mechanisms which fall beyond the scope of experiments and theories. A variety of numerical models, such as molecular dynamics simulation (MD),[10–13] direct simulation of Monte Carlo (DSMC),[14,15] lattice Boltzmann method (LBM),[16,17] and traditional computational fluid dynamics (CFD), have been widely applied to the studies of micro-gaseous flow. Due to expensive computational costs, MD and DSMC have extremely restricted applications on a macroscale. The traditional continuum-based CFD models are of limited applicability to the rarefied gas flows where continuum assumption

*Project supported by the Strategic Program of Chinese Academy of Sciences (Grant No. XDB10030400), the Hundred Talent Program of Chinese Academy of Sciences (Grant No. Y323081C01), and the National Natural Science Foundation of China (Grant No. 51439008).

†Corresponding author. E-mail: scdeng@whrsm.ac.cn

© 2019 Chinese Physical Society and IOP Publishing Ltd

breaks down (e.g., $Kn > 0.1$). The LBM, originating from the kinetic theory of molecules,[18,19] is a mesoscopic numerical model. It achieves considerable success in modeling the near continuum regime flows ($Kn < 0.1$), and has been tried in previous studies to treat rarefied gas flows in transition flow regimes within straight channels.[20–29] A series of LBM-based models with kinetic boundary schemes has been proposed to address micro-gaseous flow over curved surfaces in the slip and early transition flow regime.[30–38] Karlin *et al.*[35] first proposed a discrete form of the completely diffusive reflection, which can be applied to curved walls, but some studies revealed that this boundary overestimates the slip velocity at the wall for micro-Poiseuille flow. Following Karlin *et al.*'s work, a combination form of diffusive reflection and bounce-back scheme (namely the DBB scheme), proposed by Luo *et al.*[34] and Chai *et al.* almost at the same time,[32] has been used to model micro-gaseous flow in complex pores. In the DBB scheme, the 1st-order[34] or 2nd-order velocity-slip boundary condition[32] was incorporated into the LBM model by choosing an appropriate combination coefficient. The studies of Tao and Guo *et al.* expanded the applications of the DBB scheme to micro-flows over spheres in slip and early transition regimes.[33,37,38]

To date, despite the fruitful achievements in predicting the micro-gaseous flow in slip and early transition flow regimes via LBM-based models, little attention has been paid to the LBM-based modeling of the coupled multi-scale and multi-mechanism flow. The strategies appearing in previous literature can be summarized into five categories in terms of LBM-based modeling for the micro-gaseous flow considering surface diffusion. In the first category, the Langmuir slip model is incorporated into the LBM.[39–41] By using the non-equilibrium extrapolation scheme,[42] Fathi *et al.*[39] first developed an LBM-based boundary scheme to capture the multi-mechanism flow. Wang *et al.*[40] developed a similar boundary to account for the Langmuir slip model. In the boundary scheme of Wang *et al.*, the strategies of Inamuro *et al.*[43] were used to handle the surface diffusion, and the slip velocity of free gas near to the wall was determined by a kinetic boundary scheme. However, extending their boundary scheme into inclined wall or curved wall was difficult for several reasons. Wang *et al.*[41] presented a new boundary scheme to take account of Langmuir slip boundary by utilizing the non-equilibrium extrapolation approach.[42] Again, only the cases with straight channels were validated and tested in their studies. In the second category, long-range forces are introduced into the LBM to consider gas adsorption/desorption and boundary slip (see Refs. [10], [39], [44], and [45] for details). In their studies, gas adsorption/desorption in organic pores was modeled by long-range forces between gas and wall, and the velocity-slip induced by micro-scale effect and rarefaction effect was simulated by kinetic boundary schemes. Nevertheless, the selection of some micro-parameters of long-range forces in these models, e.g., the interaction strength between gas and wall, wall's density, is a challenging task. In the third category, some semi-analytical or analytical models are incorporated into the LBM.[46–49] Chen *et al.*[46] proposed a generalized LBM model to simulate the flow through a representative elementary volume (REV) scale porous medium considering the Klinkenberg's effect, based on the permeability correction in drag force, then an REV-scale LBM model was developed to approach the multi-mechanism flow in the reconstructed shale matrix.[47,48] In the fourth category, the surface diffusion is considered as a moving boundary.[50–52] Ren *et al.*[50,53] developed the BSR or DBB boundary with a moving wall to study the coupling effect of micro-scale flow and surface diffusion, and the velocity of the moving wall equals the adsorbed-gas transport velocity. However, the constant pressure gradient was employed in their study to calculate the adsorbed-gas transport velocity, which did not reflect the real cases with complicated geometries. In the fifth category, the LBM and other numerical methods are coupled,[10,11] e.g., molecular dynamics.

As pointed out above, the LBM-based modeling for micro-gaseous flow considering surface diffusion in irregular organic-rich pores is still in its vacancy. In this study, a more accurate model is developed to address this issue and overcomes some existing defects. The rest of this paper is organized as follows. In Section 2, we introduce our LBM numerical model, LBM-based boundary scheme, algorithm to extend the present scheme to the cases involving irregular pores, and validations by benchmarking cases. In Section 3, we present extensive parametric studies on the micro-scale flow in a self-developed tree-like model considering surface diffusion. In Section 4, we draw some conclusions and point out the future research directions.

2. Lattice Boltzmann method and boundary conditions

2.1. D2Q9 single-relaxation-time LBM model

The lattice Boltzmann method is a mesoscopic numerical method for computational fluid dynamics. Using the multi-scale analysis developed by Chapman and Enskog, the Navier–Stokes equations can be recovered from the lattice Boltzmann equation. The expression of the lattice Boltzmann equation with external force can be given as follows:

$$f_i(x + c_i\delta_t, t + \delta_t) - f_i(x,t) = \Omega(f_i) + \delta t F_i, \tag{1}$$

where $f_i(x,t)$ is the particle distribution function, δ_t is the time increment, the term $\Omega(f_i)$ on the right-hand side is the collision operator, and F_i is the external force in the i-th direction,

which is defined as

$$F_i = w_i\left(1-\frac{1}{2\tau_s}\right)\left[\frac{\boldsymbol{c}_i\cdot\boldsymbol{G}}{c_s^2}+\frac{\boldsymbol{uG}:\left(\boldsymbol{c}_i\boldsymbol{c}_i-c_s^2\boldsymbol{I}\right)}{c_s^4}\right],$$

with $\boldsymbol{G}$ being the external force in physical model.

This study adopts D2Q9 model to predict the gas flow through a porous medium. Its velocity directions are defined as: $\boldsymbol{c}_0=(0,0)$, $\boldsymbol{c}_1=(1,0)$, $\boldsymbol{c}_2=(-1,0)$, $\boldsymbol{c}_3=(0,1)$, $\boldsymbol{c}_4=(0,-1)$, $\boldsymbol{c}_5=(1,1)$, $\boldsymbol{c}_6=(-1,-1)$, $\boldsymbol{c}_7=(1,-1)$, and $\boldsymbol{c}_8=(-1,1)$.

Usually, the collision operator $\Omega(f_i)$ is a nonlinear integral differential expression in terms of particle distribution function $f_i(x,t)$. The well-known linearized collision operator $\Omega(f_i)$ is employed and expressed as[16]

$$\Omega(f_i) = -\frac{1}{\tau_s}\left[f_i(x,t)-f_i^{(\mathrm{eq})}(x,t)\right], \tag{2}$$

where τ_s is the non-dimensional relaxation time, and $f_i^{(\mathrm{eq})}(x,t)$ is the equilibrium distribution function. The above lattice Boltzmann equation (Eq. (1)) combined with Eq. (2) is called the lattice Bhatnagar–Gross–Krook (LBGK) model, in which $f_i^{(\mathrm{eq})}(x,t)$ is given as

$$f_i^{(\mathrm{eq})}(x,t) = w_i\rho\left[1+\frac{\boldsymbol{c}_i\cdot\boldsymbol{u}}{c_s^2}+\frac{\boldsymbol{uu}:\left(\boldsymbol{c}_i\boldsymbol{c}_i-c_s^2\boldsymbol{I}\right)}{2c_s^4}\right], \tag{3}$$

where w_i is the weight, and c_s is the sound speed of the lattice, and ρ and $\boldsymbol{u}$ are the density and velocity of the fluid, respectively.

The macroscopic quantities, e.g., density ρ, velocity $\boldsymbol{u}$, and pressure p, can be expressed in terms of distribution function $f_i(x,t)$ as follows:

$$\rho=\sum_{i=0}^{8} f_i, \quad \boldsymbol{u}=\frac{1}{\rho}\sum_{i=0}^{8} f_i\boldsymbol{c}_i, \quad p=\rho c_s^2. \tag{4}$$

The relationship between kinematic viscosity v and relaxation time τ_s can be obtained to be

$$v = c_s^2\left(\tau_s-0.5\right)\delta_t.$$

For the micro-scale flow, the widely recognized dimensionless parameter is the Knudsen number (Kn), which is defined as the ratio of the mean free path of gas molecules over the characteristic length. The relaxation time can be determined by the Knudsen number to be

$$\tau_s = 0.5+Kn\cdot H\cdot\sqrt{6/\pi}, \tag{5}$$

where H is the characteristic length.

2.2. Boundary condition considering surface diffusion

The adsorbed methane gas and free gas are coexistent in organic-rich pores. An accurate description of the coupling process of micro-gaseous flow and surface diffusion induced by adsorbed gas is under development and still has a puzzle. The universally adopted Langmuir slip model[39–41,54,55] is introduced to obtain the resultant slip velocity $\boldsymbol{u}_s$ at wall. It can be expressed as

$$\boldsymbol{u}_s = \theta\boldsymbol{u}_w+(1-\theta)\boldsymbol{u}_g, \tag{6}$$

where $\boldsymbol{u}_w$ is the diffusion velocity induced by the surface diffusion, and $\boldsymbol{u}_g$ is the slip velocity adjacent to the wall, and θ is the fractional coverage of adsorbed gas in thermal equilibrium.[56] The fractional coverage of adsorbed gas satisfies the following relation:

$$\theta = \frac{bp}{1+bp}, \tag{7}$$

where b is the Langmuir constant, and p is the pressure of free gas.

We determine the diffusion velocity of adsorbed gas at wall with the strategies that combine the Maxwell–Stefan approach and Langmuir adsorption isotherm,[40] the effectiveness of which has been validated and confirmed by experimental and simulation studies. The diffusion velocity is expressed as[40]

$$\boldsymbol{u}_w = \frac{q_{\mathrm{sat}}M}{\rho_{\mathrm{ads}}}\frac{bD_s}{1+bp}\nabla p, \tag{8}$$

where q_{sat} is the Langmuir volume, ρ_{ads} is the density of adsorbed gas, D_s is the Maxwell–Stefan diffusivity, M is the molecular weight of adsorbed gas, which equals 16×10^{-3} kg/mol for methane, and the definitions of b and p are shown in Eq. (7).

2.3. Self-developed boundary scheme considering surface diffusion

Note that three kinds of velocities are introduced into this study: the resultant slip velocity $\boldsymbol{u}_s$, the slip velocity $\boldsymbol{u}_g$, and the surface diffusion velocity $\boldsymbol{u}_w$, as shown in Eq. (6). Next, we develop an LBM-based boundary scheme that combines with the aforementioned Langmuir boundary scheme (Eq. (6)) to capture the coupled effect of multi-scale and multi-mechanism flow in porous medium. Inspired by previous research,[40,41,50,51] in which the surface diffusion was regarded as a moving wall, in this work we employ the non-equilibrium extrapolation scheme[42] to accurately impose the prescribed velocity $\boldsymbol{u}_w$ at the wall. The slip velocity $\boldsymbol{u}_g$ can be determined by some LBM-based kinetic boundaries, e.g., the discrete Maxwellian (DM),[35] the combined bounce-back scheme and specular reflection (BSR),[57] and DBB.[31,32,35] We eventually employ the DBB boundary scheme[31] to introduce the 2nd-order velocity-slip boundary scheme into SRT-LBM for capturing micro-gaseous flow in regular/irregular pores in this study.

The idea of non-equilibrium extrapolation scheme is that the unknown distribution functions of boundary nodes are approximated with the results of adjacent fluid nodes. At time step t, after collision and streaming step, the unknown distribution functions of a boundary node $x_{\rm b}$ are decomposed into two parts as follows:[58]

$$f_i(x_{\rm b},t) = f_i^{(\rm eq)}(x_{\rm b},t) + f_i^{(\rm neq)}(x_{\rm b},t). \tag{9}$$

The equilibrium part $f_i^{(\rm eq)}(x_{\rm b},t)$ is approximated with that of its adjacent fluid node as

$$f_i^{(\rm eq)}(x_{\rm b},t) = f_i^{(\rm eq)}\left(\rho\left(x_{\rm f}\right),\boldsymbol{u}_{\rm w}\right), \tag{10}$$

where $x_{\rm f} = x_{\rm b} + \boldsymbol{c}_i\delta_t$, and $\boldsymbol{u}_{\rm w}$ is the known diffusion velocity given by Eq. (8). The non-equilibrium part of the unknown distribution function is determined by that of its adjacent fluid node $x_{\rm f} = x_{\rm b} + c_i\delta_t$ to be

$$f_i^{(\rm neq)}(x_{\rm b},t) = f_i(x_{\rm f},t) - f_i^{(\rm eq)}(x_{\rm f},t). \tag{11}$$

After obtaining the unknown distribution functions of boundary nodes at time step t, the unknown distribution functions of adjacent fluid nodes at time step $t+1$ can be provided by the collision and streaming of their adjacent boundary nodes, which can be expressed as

$$\begin{aligned} &f_i(x_{\rm f},t+\delta_t) = f_i'(x_{\rm b},t) \\ &= f_i^{(\rm eq)}\left(\rho,\boldsymbol{u}_{\rm w}\right) + \frac{\tau_{\rm s}-1}{\tau_{\rm s}}\left(f_i(x_{\rm f},t) - f_i^{(\rm eq)}(x_{\rm f},t)\right), \end{aligned} \tag{12}$$

where $f_i'(x_{\rm b},t)$ indicates the post-collision distribution function of boundary nodes, and is expressed as

$$f_i'(x_{\rm b},t) = f_i(x_{\rm b},t) - \frac{1}{\tau_{\rm s}}\left(f_i(x_{\rm b},t) - f_i^{(\rm eq)}(x_{\rm b},t)\right).$$

The halfway DBB boundary scheme developed by Chai *et al.*[31] is adopted in this study to determine the velocity slip $\boldsymbol{u}_{\rm g}$ at the wall. It can be expressed as

$$f_i = rKf_i^{\rm eq}(\rho_{\rm w},\bar{\boldsymbol{u}}_{\rm w}) + (1-r)f_{\bar{i}}', \tag{13}$$

where $\bar{i}$ represents the opposite direction of i, $r$is the combination parameter, and $\rho_{\rm w}$ and $\bar{\boldsymbol{u}}_{\rm w}$ are the density and velocity of the wall, respectively. And K is the normalization factor to ensure mass conservation, and can be expressed as

$$K = \frac{\sum_{\boldsymbol{\xi}_i'\cdot\boldsymbol{n}<0}|\boldsymbol{\xi}_i'\cdot\boldsymbol{n}|f_i'}{\sum_{\boldsymbol{\xi}_i'\cdot\boldsymbol{n}>0}|\boldsymbol{\xi}_i'\cdot\boldsymbol{n}|f_i^{\rm eq}(\rho_{\rm w},\boldsymbol{u}_{\rm w})}, \quad \boldsymbol{\xi}_i' = \boldsymbol{c}_i - \bar{\boldsymbol{u}}_{\rm w}, \tag{14}$$

where f_i' is the post-collision distribution function given as $f_i' = f_i - \frac{1}{\tau_{\rm s}}\left(f_i - f_i^{(\rm eq)}\right)$, and $\boldsymbol{n}$ is the wall's normal vector.

Considering Eq. (14), for a static wall (namely, $\bar{\boldsymbol{u}}_{\rm w} = 0$), the DBB boundary scheme (Eq. (13)) can be simplified as

$$f_i = r\cdot\frac{w_i}{\sum_j w_j}\sum_j f_j' + (1-r)f_{\bar{i}}', \tag{15}$$

where $\sum_j f_j'$ represents the sum of post-collision distribution functions streaming toward solid nodes, and $\sum_j w_j$ is the sum of the weights of outgoing distribution functions.

To include the 2$^{\rm nd}$-order slip boundary condition (e.g., $\boldsymbol{u}_{\rm g} = C_1\lambda\left(\partial u/\partial\boldsymbol{n}\right)_{\rm s} - C_2\lambda^2\left(\partial^2 u/\partial\boldsymbol{n}^2\right)_{\rm s}$), the combination parameter r should be chosen as for the single-relaxation-time model[31]

$$r = \frac{2}{1+\dfrac{4\sqrt{6/\pi}Kn}{4C_1Kn+8C_2Kn^2-32Kn^2/\pi+\Delta^2}}, \tag{16}$$

where $\Delta = 1/H$ with H being the local characteristic length.

By combining Eqs. (15) and (12), we develop an LBM-based boundary scheme to implement the Langmuir slip boundary given by Eq. (6) in the LBM framework. This self-developed boundary scheme can be presented as

$$\begin{aligned} &f_i(x_{\rm f},t+\delta_t) \\ &= \theta\left(f_i^{(\rm eq)}\left(\rho\left(x_{\rm f},t\right),\boldsymbol{u}_{\rm w}\right) + \frac{\tau_{\rm s}-1}{\tau_{\rm s}}\left(f_i(x_{\rm f},t) - f_i^{(\rm eq)}(x_{\rm f},t)\right)\right) \\ &\quad + (1-\theta)\cdot\left(r\cdot\frac{w_i}{\sum_j w_j}\sum_j f_j'(x_{\rm f},t) + (1-r)f_{\bar{i}}'(x_{\rm f},t)\right). \end{aligned} \tag{17}$$

The boundary scheme (Eq. (17)) can be applied to the tree-like porous medium due to its independence of the normal vector of the wall.

2.4. Regularization procedure

To ensure that the present SRT-LBM scheme is more accurate and stable in the hydrodynamic regime, a regularization step, developed by previous studies,[59–61] is embedded into this model to capture micro-gaseous flow at high Knudsen number. It filters out unnecessary higher-order contributions to non-equilibrium distribution functions to ensure that the non-equilibrium moments of the distribution functions satisfy the Hermite space.[60] The distribution functions are decomposed into the equilibrium and non-equilibrium parts as[60]

$$f_i(x,t) = f_i^{(\rm eq)}(x,t) + f_i^{(\rm neq)}(x,t). \tag{18}$$

The non-equilibrium part $f_i^{(\rm neq)}(x,t)$ can be converted into

$$\bar{f}_i^{(\rm neq)}(x,t) = w_i\left[\frac{1}{2c_{\rm s}^2}He_{mn}^{(2)}\left(\frac{\boldsymbol{c}_i}{c_{\rm s}}\right)\sum_{k=0}^{8}f_k^{(\rm neq)}c_{km}c_{kn}\right], \tag{19}$$

where $He_{mn}^{(2)}(\boldsymbol{\xi}) = \xi_m\xi_n - \delta_{mn}$ with δ_{mn} being the Kronecker delta function, $f_k^{(\rm neq)}(x,t) = f_k(x,t) - f_k^{(\rm eq)}(x,t)$, subscripts m, n are the dummy indexes which obey the Einstein's summation convention, $\boldsymbol{c}_i$ is the discrete velocity of D2Q9, just as shown in Subsection 2.1, and c_{kn} is the n-th direction of discrete velocity $\boldsymbol{c}_k$.

The evolution equation for the SRT-LBM model after being regularized is given as

$$\begin{aligned} &f_i(x+c_i\delta_t,t+\delta_t) \\ &= f_i^{(\rm eq)}(x,t) + \bar{f}_i^{(\rm neq)}(x,t) - \frac{1}{\tau_{\rm s}}\bar{f}_i^{(\rm neq)}(x,t). \end{aligned} \tag{20}$$

2.5. Local Knudsen number and local pressure gradient

For the micro-gaseous flow in a porous medium, the Knudsen number is a local geometry-dependent parameter and associated with space location due to the spatial variation of its influencing factors, such as temperature, gas pressure, local characteristic length, etc.

For the hard sphere molecule, the mean free path λ of gas molecule can be expressed as[36]

$$\lambda = \frac{m}{\sqrt{2}\pi\rho\sigma^2}, \tag{21}$$

where m and ρ are the molecule mass and gas density, respectively, and σ is the molecule diameter.

With Eq. (21), the Knudsen number for ideal gas is given as

$$Kn_{\rm loc} = \frac{\lambda}{H_{\rm loc}} = \frac{m}{\sqrt{2}\pi\rho_{\rm loc}\sigma^2 H_{\rm loc}} = \frac{RT}{\sqrt{2}\pi P_{\rm loc} N_{\rm A}\sigma^2 H_{\rm loc}}, \tag{22}$$

where R and T are the gas constant and temperature, respectively, $N_{\rm A}$ is the Avogadro constant, $P_{\rm loc}$ and $H_{\rm loc}$ are the local pressure of gas and local characteristic length of porous medium, respectively, and they are determined by the following strategies. Equation (22) indicates that the product of local Kn, local pressure, and local characteristic length keeps constant for isothermal flow.

For pressure-driven micro-flows, the pressure gradient is also a space-dependent local parameter. To accurately capture surface diffusion and micro-scale flow along the surface, inspired by the research of Zhao *et al.*,[10,36] we propose a method to determine the local characteristic length and pressure gradient of free gas based on the following hypotheses: 1) the pressure variation of free gas along the transverse (or spanwise) direction can be neglected under an extremely low pressure difference at inlet and outlet; 2) the pressure gradient of free gas can be approximated by that of its nearest skeleton node of pore structures according to hypothesis 2); 3) the characteristic length of a fluid node equals that of its nearest skeleton node of pore structures, which can be reasonably accepted due to the definitions of the node's characteristic length and skeleton of pore structures.

The detailed methods to approximately obtain the local characteristic length and pressure gradient of free gas are given below.

(I) The first step is to obtain the skeleton of pore structures. A thinning algorithm for digital patterns proposed by Zhang *et al.*[62] is employed in this study. It consists of two subiterations, aiming at deleting boundary points to obtain the skeleton of unitary thickness for random pore structures. A random porous medium and its skeleton line are shown in Fig. 1.

(II) After obtaining the skeleton of pore structure, the local characteristic length of a skeleton point is determined by the maximal ball algorithm,[63] and then the local characteristic length of a fluid node is obtained under hypothesis 3).

(III) The pressure gradient of skeleton points is approximately obtained with difference approximation to partial derivatives, and then the pressure gradient of free gas is given by hypothesis 2).

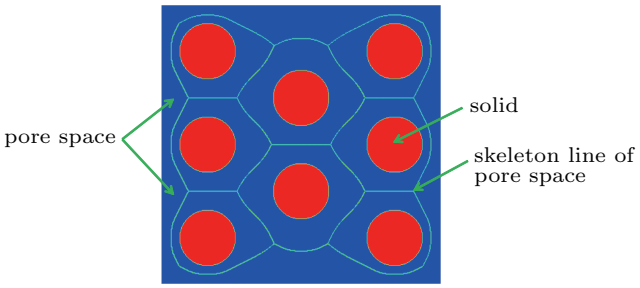


Fig. 1. A channel filled with circular cylinders and calculated skeleton line by Zhang's algorithm: the porous media and skeleton line of unitary thickness.

With the local characteristic length of fluid nodes and local pressure gradient of free gas, we can easily implement the present boundary scheme in the LBM.

A few studies and numerical research[10,11,39–42,44,50–52] focused on the LBM-based modeling of multi-mechanism flow in micro/nanopores. However, most of them were only applied to a straight channel due to some limitations. The present scheme is built by coupling the non-equilibrium extrapolation scheme and halfway DBB boundary scheme, and later used to model multi-mechanism flow in a tree-like porous medium for its independence of the wall's normal vector. The local Knudsen number for a fluid node and local pressure gradient along the skeleton line are also calculated to capture complex micro-flows along the irregular organic-rich pores. In addition, by considering viscosity correction and regularization procedure, the present model is capable of addressing high-Knudsen-number gas flows.

2.6. Model validation

2.6.1. Micro-gaseous flow in periodic microchannel

The micro-gaseous flow in a two-dimensional (2D) microchannel is employed to validate the proposed boundary scheme with Kn over a wide range. The gas flow is driven by a constant pressure gradient of $\partial p/\partial x = 10^{-4}$, and the inlet and outlet are set as periodic boundary. The embedded Langmuir slip boundary (Eq. (17)) is imposed at the bottom and top walls with $\theta = 0$. The slip coefficients of the 2nd-order velocity-slip boundary are chosen to be $C_1 = 1.1466$ and $C_2 = 0.9757$ for a full diffusive wall. The size is set to be $N_x = 50$ and $N_y = 51$, which is large enough to obtain grid-independence results. To compare with the results of Ohwada *et al.*,[64] micro-Poiseuille flows are carried out at $Kn = \left(2/\sqrt{\pi}\right)k$ with $k = 0.1, 0.2, 0.4, 1.0$. The relaxation time in Eq. (5) is corrected as $\tau_{\rm s} = 0.5 + Kn \cdot \frac{H}{(1+2Kn)} \cdot \sqrt{\frac{6}{\pi}}$ to capture rarefaction effects.

The streamwise velocity profiles at four Knudsen numbers are presented in Fig. 2, where the dimensionless streamwise velocity U is defined as $U = u/u_{\text{ave}}$, with $u_{\text{ave}} = 1/H \int_0^H u\mathrm{d}y$. Only slight differences are found between our results and those of Ohwada *et al.*,[64] although the discrepancies increase with the value of Kn increasing.

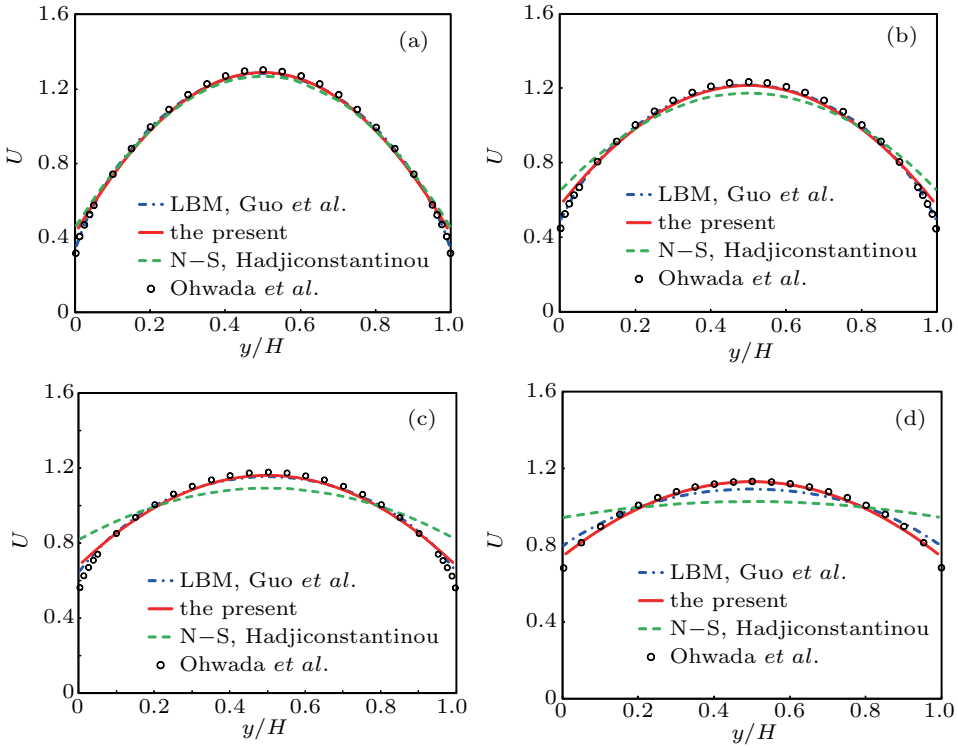


Fig. 2. Streamwise velocity profiles of micro-scale gas flow when Knudsen number varies in a wide range. Our numerical results are compared with those of Ohwada *et al.*,[64] Hadjiconstantinou *et al.*,[75] and Guo *et al.*[21] for (a) $Kn = 0.1128$, (b) $Kn = 0.2257$, (c) $Kn = 0.4514$, and (d) $Kn = 1.1284$.

2.6.2. Pressure-driven micro-gaseous flow in long microchannels

Gas flow driven by constant pressure gradient is the ideal case. However, the pressure-driven gas flow is more ubiquitous and significant in engineering applications. The micro-gaseous flow driven by pressure difference was modeled and validated in previous studies.[34,65] In this section, following the previous study,[65] we simulate the gas flow in a two-dimensional (2D) microchannel with height H and length L, and it is driven by a pressure difference between inlet pressure p_{in} and outlet pressure p_{out}. For isothermal micro-gaseous flow in the microchannel where the characteristic length of each fluid node is the height H, equation (22) can be further reduced into $Kn(x) = \frac{Kn_{\text{out}} p_{\text{out}}}{p(x)} = \frac{Kn_{\text{in}} p_{\text{in}}}{p(x)}$, where Kn_{in} and Kn_{out} are the Knudsen numbers at inlet and outlet, respectively, and $p(x)$ is the pressure along the channel centerline. To compare with existing results, we choose two Knudsen numbers: $Kn_{\text{out}} = 0.0194, 0.194$.

The size is set to be $N_x = 2000$ and $N_y = 20$ to ensure that the ratio of length over height is 100. The top and bottom walls are treated by the proposed boundary scheme, and the strategies of Verhaeghe *et al.*[34] are taken to address the pressure boundary at inlet and outlet. The outlet pressure p_{out} is 1.0 / 3.0, and inlet pressure p_{in} is set to be 1.4 / 3.0 for $Kn = 0.0194$ and 2.0 / 3.0 for $Kn = 0.194$. Figure 3 shows the normalized velocity $u/u_{\max}$ at the outlet and dimensionless pressure deviation along the long microchannel when $Kn = 0.0194$, 0.194. The pressure deviation from linear pressure distribution p_l along the streamwise direction is given as

$$\delta p = \frac{p(x) - p_l}{p_{\text{out}}},$$
$$p_l = p_{\text{in}} + (p_{\text{out}} - p_{\text{in}})x/L,$$

where $L = N_x$ presents the microchannel length.

In Fig. 3(a), the streamwise velocity and pressure deviation from linear pressure profiles match well with the results of IP-DSMC[66] when $Kn = 0.0194$. Figure 3(b) shows the corresponding results at $Kn = 0.194$, and good agreement between the present results and those of IP-DSMC,[66] which validates the effectiveness of the present scheme in predicting microchannel flow.

2.6.3. Validations of present boundary scheme

In the above two subsections, we verify that this boundary scheme is capable of modeling the micro-gaseous flow in slip and early transition flow regimes in a straight channel. In this subsubsection, we mainly check its accuracy and effectiveness in simulating the micro-scale gas flow considering surface diffusion. To include some existing results[40,41] for better comparison, we assume that $\boldsymbol{u}_{\text{w}} = \alpha \boldsymbol{u}_{\text{g}}$, where $0 \le \alpha \le 1$. Under this assumption, equation (6) can be reduced to

$$\begin{aligned} &\boldsymbol{u}_{\rm s} = \theta\alpha\boldsymbol{u}_{\rm g} + (1-\theta)\boldsymbol{u}_{\rm g}, \\ &0 \le \theta \le 1, \\ &0 \le \alpha \le 1. \end{aligned} \tag{23}$$

And $\boldsymbol{u}_{\rm g}$ is determined by the 2nd-order velocity-slip boundary scheme to be

$$\boldsymbol{u}_{\rm g} = C_1\lambda\left(\frac{\partial u}{\partial \boldsymbol{n}}\right)_{\rm s} - C_2\lambda^2\left(\frac{\partial^2 u}{\partial \boldsymbol{n}^2}\right)_{\rm s}, \tag{24}$$

where u is the velocity of free gas.

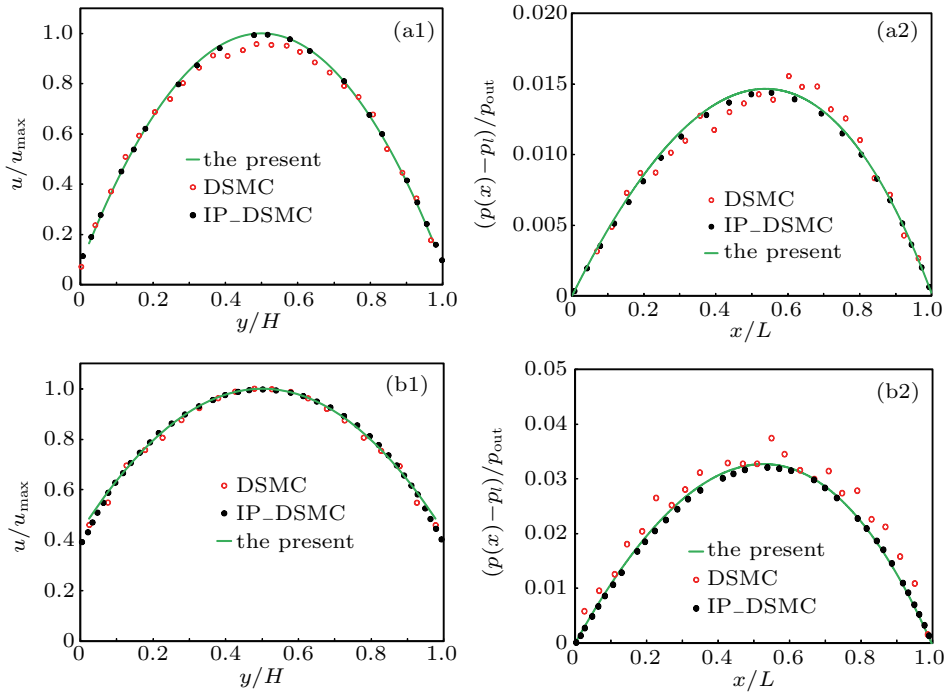


Fig. 3. Normalized streamwise velocity profiles at outlet and non-dimensional pressure deviation along microchannel for (a) $Kn = 0.0194$ and (b) $Kn = 0.194$. Our numerical results are compared with results of Shan *et al.*[66]

Then by combining Eqs. (24) and (23), the governing equation and boundary schemes for micro-gaseous flow in a single organic pore can be expressed as

$$\begin{aligned} &\frac{\partial^2 \boldsymbol{u}}{\partial y^2} = -\frac{1}{\mu}\frac{\partial p}{\partial x}, \\ &\boldsymbol{u}|_{y=0,H} = \theta\alpha\boldsymbol{u}_{\rm g} + (1-\theta)\boldsymbol{u}_{\rm g}, \\ &\boldsymbol{u}_{\rm g} = C_1\lambda\left(\frac{\partial u}{\partial \boldsymbol{n}}\right)_{\rm s} - C_2\lambda^2\left(\frac{\partial^2 u}{\partial \boldsymbol{n}^2}\right)_{\rm s}, \end{aligned} \tag{25}$$

where $\partial p/\partial x$ is the pressure gradient, and $\mu = \rho\nu$ is the dynamic viscosity.

The analytical solution of Eq. (25) can be obtained to be

$$\begin{aligned} \boldsymbol{u} = &\frac{(-\partial p/\partial x)\cdot H^2}{2\mu}\frac{y}{H}\cdot\left(1-\frac{y}{H}\right) + \frac{(-\partial p/\partial x)\cdot H^2}{8\mu} \\ &\times(\theta\alpha+(1-\theta))\cdot\left(4C_1Kn + 8C_2Kn^2\right), \end{aligned} \tag{26}$$

where $Kn = \lambda/H$.

In this subsubsection, the present boundary scheme (Eq. (17)) is used to study multi-mechanism flow, including micro-scale gas flow and surface diffusion, and then it is further validated by our analytical solution (Eq. (26)). As stated by Lee *et al.*[67] and Li *et al.*,[65] the case with the infinitely long microchannel can be simplified into a periodic channel, which is reasonably used in this subsubsection.

We first choose the case with $Kn = 0.0729$ and $\theta = 1.0$ to make comparisons with the existing results.[40,41] The size is set to be $N_x = 2$ and $N_y = 500$ for the periodic microchannel in use, and it is proven that this mesh size satisfies the mesh-independence. Figure 4 shows the streamwise velocity profiles at outlet, where $Y = y/H$ and $U = u/u_{\max}$ with $u_{\max}$ being the maximum velocity at outlet. The detailed comparisons between our numerical results, the results of Wang *et al.*[40] and Wang *et al.*,[41] and analytical solutions (Eq. (26)) are presented in this figure. It can be observed that the streamwise velocity profiles predicted by the present boundary match well with the analytical results, and it is also superior to the boundary schemes proposed by Wang *et al.*[40] and Wang *et al.*,[41] which cannot effectively predict the velocity at the wall. Wang *et al.*'s boundary scheme[40] tends to overestimate the streamwise velocity at large diffusion velocity, and Wang *et al.*'s boundary scheme[41] overestimates the velocity at the wall for all cases. It seems that the latter will introduce some unphysical velocity at the wall. To clearly show the differences, the velocities at walls predicted by four models are also given in Table 1, showing a maximum relative error of 1.85% between our results and analytical solutions, noticeably lower than those of Wang *et al.*[40,41] Specifically, our relative errors are about one order of magnitude smaller than those of Wang

et al.[40,41] under the same conditions. For the internal microflows, the accurate capturing for the velocity at wall is critical for modeling the flow and permeability prediction. Moreover, Wang *et al.*'s model[40] is not applicable to the inclined channel (or curved wall) due to the limitations of Inamuro *et al.*'s boundary scheme.[43] In contrast, the present boundary scheme has a higher accuracy and the capability of addressing irregular pores, such as tree-like porous media in this study.

As is well known, the SRT-LBM model with bounce-back boundary will give rise to the viscosity-dependent unphysical issue when predicting velocity or permeability.[58,68–70] Actually, it is not induced by the SRT-LBM model, but by the bounce-back boundary and discretization errors.[18,69] The bounce-back boundary generally introduces an unphysical velocity-slip at static wall, which is associated with τ_s $\left(\tau_s = \frac{\nu}{c_s^2 \delta_t} + 0.5\right)$ and proportional to Δ^2,[58] so it is responsible for this viscosity-dependent unphysical issue. It should be noted that this unphysical issue also exists in the MRT-LBM model if improper relaxation time τ_q is chosen. However, the present boundary scheme (Eq. (17)) is developed by combining the non-equilibrium extrapolation scheme and halfway DBB scheme. The fact that both of them accurately impose the prescribed velocity at wall ensures its effectiveness.

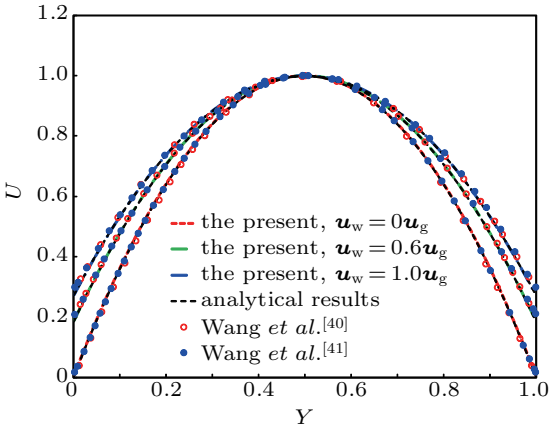


Fig. 4. Comparison among the non-dimensional velocity profile predicted by the present model, analytical result, and previous studies (Wang *et al.*[40] and Wang *et al.*[41]) when $Kn = 0.0729$ and $\theta = 1.0$.

Table 1. Normalized velocities at wall ($\boldsymbol{u}_s$) predicted by different models, and the relative errors (in parentheses) between calculated results and analytical solutions when $Kn = 0.0729$ and $\theta = 1$. The relative errors are calculated as $\left|\frac{\boldsymbol{u}_s - \boldsymbol{u}_s^{ana}}{\boldsymbol{u}_s^{ana}}\right| \times 100\%$, with $\boldsymbol{u}_s^{ana}$ being the analytical solutions.

α	Analytical solutions	Present model	Wang *et al.*[40]	Wang *et al.*[41]
0.0	0	5.074×10^{-3}	9.744×10^{-3}	1.462×10^{-2}
0.6	0.1840	0.1874 (1.85)	0.2039 (10.8)	0.2071 (12.6)
1.0	0.2732	0.2732 (< 0.1)	0.2940 (7.61)	0.2996 (9.66)

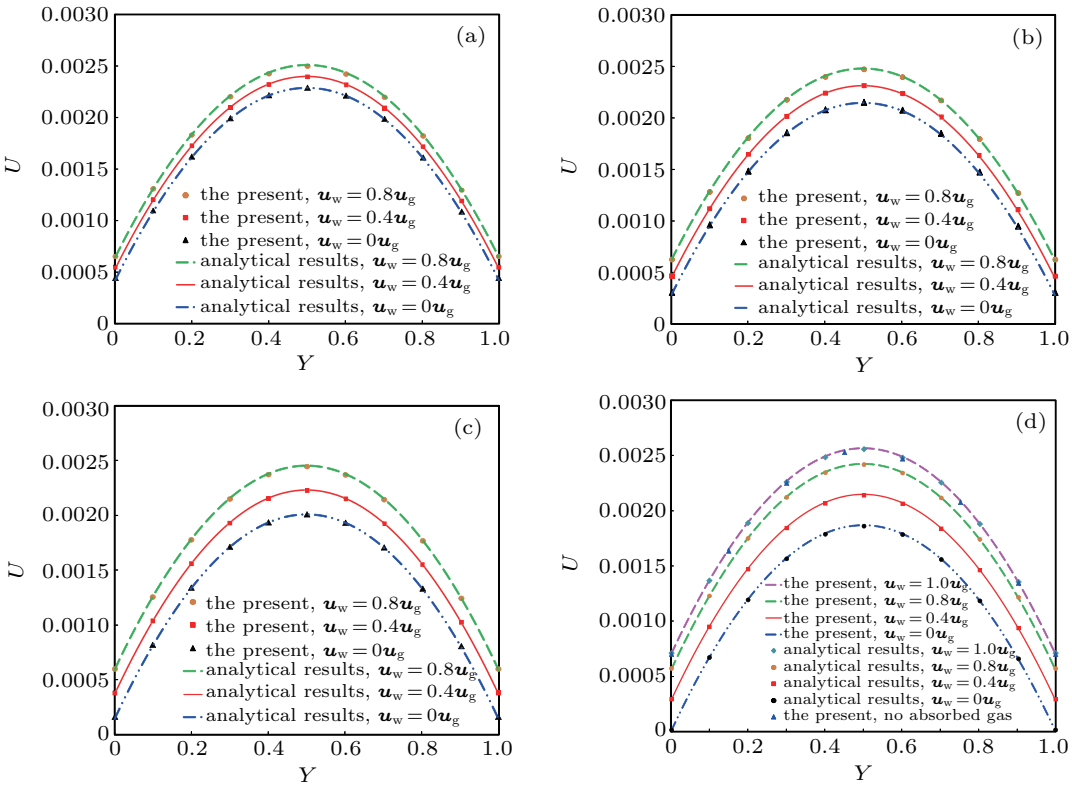


Fig. 5. Comparison between streamwise velocity profiles predicted by the present model and analytical results (Eq. (26)) when $Kn = 0.0729$ and (a) $\theta = 0.4$, (b) $\theta = 0.6$, (c) $\theta = 0.8$, and (d) $\theta = 1.0$.

To further validate the proposed model, we carry out a series of validation cases with Kn (viscosities) and θ over a wide range. Our results are then compared with the analytical results from Eq. (26). The model and boundary schemes are the same as the above cases. Figure 5 shows our results and analytical results when $Kn = 0.0729$ with $\theta = 0.4$–1.0 and $\alpha = 0.0$–1.0. There is very little difference in the streamwise velocity between our results and the analytical results. A comparison of Fig. 5(a) to 5(d) indicates that as expected the $\boldsymbol{u}_s$ at wall decreases with the value of $\boldsymbol{u}_w$ decreasing, and that small θ makes the effect of $\boldsymbol{u}_w$ on $\boldsymbol{u}_s$ less significant due to the small percentage of adsorbed gas. Figure 5(d) presents the case with $\theta = 1.0$, and the results when $\theta = 0.0$ and $\boldsymbol{u}_s = \boldsymbol{u}_g$ are also included for comparison. It also demonstrates that the present boundary predicts well for micro-gaseous flow in the presence or absence of adsorbed gas, and that the Poiseuille flow in the continuum limit with no-slip boundary is also accurately recovered when $\theta = 1$ and $\alpha = 0$.

In the following parts, several cases with $Kn = 0.01$–0.12, within which the micro-gaseous flow in tight gas reservoirs mainly falls, are carefully investigated to further validate the present model. Again, all settings are consistent with the above validations in this subsubsection except for Kn. Our results show good agreement with analytical results when micro-gaseous flow considering surface diffusion falls within slip and early transition flow regimes as shown in Table 2, where U_{lbm} and U_{ana} are the sum of numerical and analytical streamwise velocities, respectively. It indicates that the maximum relative error between the present results and analytical solutions is less than 2% when Kn (viscosity) is in a wide range. Additionally, the diffusion velocity $\boldsymbol{u}_w$ is accurately imposed on wall by the non-equilibrium extrapolation scheme, and with proper combination parameter r, the 2nd-order velocity-slip boundary scheme is employed to describe the micro-scale effect by halfway DBB scheme without introducing extra unphysical velocity. All these cases verify the accuracy and effectiveness of the present model.

Table 2. Relative errors of streamwise velocity between our numerical results and analytical results (Eq. (26)) when $Kn = 0.02$, 0.05, 0.12, with $\theta = 0.2$, 0.8 and $\alpha = 0.0$–0.8. The relative errors = $\left|\frac{U_{lbm}-U_{ana}}{U_{ana}}\right| \times 100\%$, with U_{ana} being the analytical solution.

Kn	$\theta = 0.2$ $\alpha = 0.0$	$\theta = 0.2$ $\alpha = 0.4$	$\theta = 0.2$ $\alpha = 0.8$	$\theta = 0.8$ $\alpha = 0.0$	$\theta = 0.8$ $\alpha = 0.4$	$\theta = 0.8$ $\alpha = 0.8$
0.02	0.328	0.242	0.160	0.777	0.652	0.531
0.05	0.596	0.397	0.203	0.837	0.518	0.263
0.12	0.729	0.298	0.112	1.71	0.786	0.194

In the following section, the micro-gaseous flow considering surface diffusion in self-developed tree-like porous medium is predicted by the present model.

3. Multi-mechanism flow in tree-like model

The real pore structures of shale and sandstone can be reconstructed by experimental methods (e.g., computed tomography and focused ion beam scanning electron microscopy), numerical approaches (e.g., quartet structure generation set), and theoretical methods.[53] The popular theoretical models[53] are the bundle-of-tubes models, regular lattice model, circular model,[71] tree-like model,[72] etc. Inspired by the Sakhaee–Pour and Bryant's works,[72] we adopt a tree-like model (see Fig. 6) to represent shale matrix in the subsequent parametric studies.

In the above sections, all physical quantities (e.g., velocity, pressure) are non-dimensional parameters in lattice units, while all parameters have a specific physical unit in this section. Table 3 shows the convention from physical units to lattice units. Only time step increment dt_{phy} is initially unknown in the physical system, and pressure p_{latt} is required to be determined in the lattice system. The other parameters in both physical and lattice systems are predetermined prior to computing. To determine the time step increment dt_{phy}, we consider the relationship between the kinematic viscosity v_{phy} in physical units and v_{latt} in lattice units

$$v_{latt} = \frac{v_{phy}}{dx^2/dt}. \tag{27}$$

Table 3. Convention from physical units to lattice units (2D case).

Physical quantities	Physical units	Lattice units	Convention
Density	ρ_{phy}	ρ_{latt}	$\rho_r = \rho_{phy}/\rho_{latt}$
Size	H_{phy} or $(H$ or $L)$	H_{latt} or $(N_y$ or $N_x)$	$dx = H_{phy}/H_{latt}$
Time increment	dt_{phy}	$dt_{latt} = 1$	$dt = dt_{phy}/dt_{latt} = dt_{phy}$
Velocity	V_{phy}	$V_{latt} = 1$	$V_r = V_{phy}/V_{latt} = dx/dt$
Viscosity	v_{phy}	$v_{latt} = (\tau_s - 0.5)/3$	$v_{latt} = v_{phy}/(dx^2/dt)$
Pressure	p_{phy}	p_{latt}	$p_r = p_{phy}/p_{latt} = \rho_r dx^2/dt^2$

Equation (27) gives the value of $\mathrm{d}t$ (namely, $\mathrm{d}t_{\mathrm{phy}}$), then $V_{\mathrm{r}} = V_{\mathrm{phy}}$ and p_{r} can be easily determined by $V_{\mathrm{r}} = \mathrm{d}x/\mathrm{d}t$ and $p_{\mathrm{r}} = \rho_{\mathrm{r}} \cdot \mathrm{d}x^2/\mathrm{d}t^2$, respectively. The detailed information is shown in Table 3. It is worth noting that the $\boldsymbol{u}_{\mathrm{w}}$ in Eq. (8) is generally calculated in physical units, and transformed into lattice units. This enables us to simplify the computation without directly converting several parameters from physical units to lattice units, such as the Langmuir volume q_{sat}, Langmuir constant b, surface diffusivity D_{s}, etc.

Figure 6 illustrates the basic set-up of this numerical model, including the geometry and boundary conditions. The size is set to be $N_x = 401$ in length L and $N_y = 401$ in height H, which corresponds to the physical model with the initial size of 75 nm in length L and 75 nm in height H. The Zou and He's boundary scheme[73] is employed to impose a pressure difference at inlet and outlet, then other boundaries are addressed with our carefully validated boundary scheme (Eq. (17)). In our cases, the gas pressure p_{out} at outlet ranges from 10 MPa to 40 MPa with an initial pressure gradient of $\nabla p = 0.1$ MPa/m along the streamwise direction at system temperature $T = 338.7$ K. The Langmuir parameters for the adsorbed gas are carefully chosen based on the Wang *et al.*'s data[40,48] summarized from existent collections predominately reported in the literature for shale. The detailed parameters and data are chosen as follows. The density of adsorbed gas at a given θ is set to be $\rho_{\mathrm{ads}} = \rho_{\mathrm{ads,sat}}\theta$ with $\rho_{\mathrm{ads,sat}}$ being 340 kg/m^3,[74] and the Maxwell–Stefan diffusivity D_{s} ranges from 10^{-8} m^2/s to 10^{-5} m^2/s. The Langmuir volume q_{sat} is given as 1000–6000 mol/m^3. The Langmuir constant b varies from 0.125 MPa^{-1} to 1.0 MPa^{-1}.

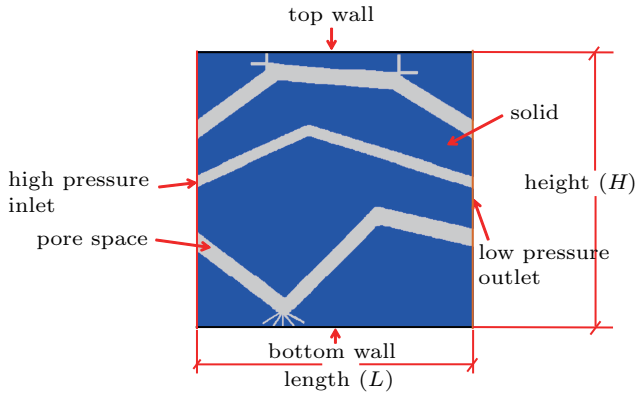


Fig. 6. Boundary conditions and geometry of tree-like model: left and right boundaries are pressure boundaries, and the present scheme (Eq. (17)) is imposed at pore surface.

In Subsection 2.5, we illustrated our strategies to obtain the local characteristic length H_{loc} and local pressure P_{loc} of free gas. The skeleton line of the tree-like model is shown in Fig. 7. Following Zhao *et al.*'s research,[10,36] we define the reference characteristic length H_{ref} and reference Knudsen number Kn_{ref} to calculate the local Knudsen number for a fluid node. The reference characteristic length of the tree-like model can be given as

$$H_{\mathrm{ref}} = \sqrt{\frac{12K_{\mathrm{abs}}}{\varepsilon}}, \tag{28}$$

where ε is the porosity of the tree-like model, and K_{abs} is its absolute permeability. They are calculated via this LBM to be $K_{\mathrm{abs}} = 4.482$ and $\varepsilon = 0.167$, then H_{ref} can be obtained to be 17.912. The Kn_{ref} associated with H_{ref} can be computed via Eq. (22) at a given gas pressure. Then, the local Knudsen number of a fluid node can be determined to be $Kn_{\mathrm{loc}} = Kn_{\mathrm{ref}}H_{\mathrm{ref}}/H_{\mathrm{loc}}(x,y)$, where we assume that the gas pressure keeps constant in determining Kn_{loc} due to the difference in pressure between inlet and outlet boundaries being extremely low.

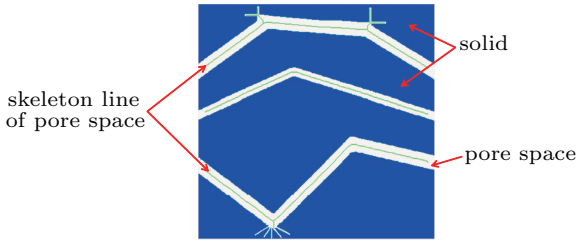


Fig. 7. Skeleton line of tree-like model. Light green line represents skeleton line obtained via the method in Subsection 2.5.

The coupling process of micro-gaseous flow and surface diffusion involves two interconnected physical mechanisms. As shown in Eq. (8), $\boldsymbol{u}_{\mathrm{w}}$ is associated with free gas pressure p, however, it in turn changes the pressure distribution of free gas. This issue is addressed by a subiteration approach, which is based on the assumption that the pressure distribution of free gas used to determine $\boldsymbol{u}_{\mathrm{w}}$ comes from the results when micro-gaseous flow reaches its mechanical equilibrium at each iteration step. It allows the execution of a number of consecutive LBM subiteration steps prior to updating $\boldsymbol{u}_{\mathrm{w}}$ at each iteration step. The detailed algorithm for this subiteration is shown in Algorithm 1 in C++ pseudocode.

The first case begins with $\nabla p = 0.1$ MPa/m, $p_{\mathrm{out}} = 10$ MPa, $D_{\mathrm{s}} = 10^{-5}$ m^2/s, $q_{\mathrm{sat}} = 4000$ mol/m^3, $b = 0.125$ MPa^{-1}, height = 75 nm and long = 75 nm. Figure 8 shows the velocity vectors of micro-gaseous flow at different values of surface diffusivity D_{s}. The results under no-slip boundary are also presented for detailed comparison. It is obvious that $\boldsymbol{u}_{\mathrm{s}}$ at solid surface becomes more visible when D_{s} varies from 10^{-8} m^2/s to 10^{-5} m^2/s. Despite its decreasing with the reduction of D_{s}, the gas velocity near to wall at extremely low D_{s} is still larger than that under no-slip boundary (see Figs. 8(c) and 8(d)), which can be attributed to the finite velocity-slip $\boldsymbol{u}_{\mathrm{g}}$.

Algorithm 1. Implementation of subiteration process of coupling effect

```
for (intiter = 0; iter <= iter_num; iter++) {     //outer loop for modeling the coupling effect;
  for(int sub_iter = 0; sub_iter <= subiter_num; sub_iter++) { // inner loop for LBM subiteration;
      if (micro-gaseous flow reaches its mechanical equilibrium state)
        {
            Update the surface diffusion velocity.
            Break the current subiteration step and continue next iteration step.
            …
        }
      else
        {
            Don't update the surface diffusion velocity.
            Continue the subiteration step.
            …
        }
        Undertake the LBM simulation
        Impose the boundary scheme given by Eq. (17).
        Impose other boundary schemes.
        …
    }
    If (micro-gaseous flow considering surface diffusion achieves convergence results)
    {
        Break the iteration step and finish the computation.
    }
  }
```

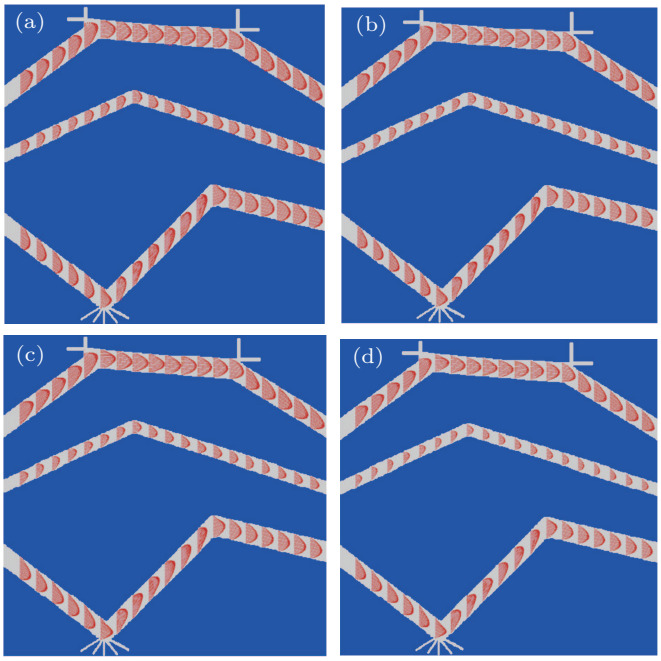


Fig. 8. Velocity vectors of micro-gaseous flow in tree-like model under different surface diffusivity values: (a) $D_s = 10^{-5}$ m^2/s, (b) $D_s = 10^{-6}$ m^2/s, and (c) $D_s = 10^{-8}$ m^2/s, and (d) flows in the continuum regime with no-slip boundary. Other parameters are $\nabla p = 0.1$ MPa/m, $p_{out} = 10$ MPa, $q_{sat} = 4000$ mol/m^3, $b = 0.125$ MPa^{-1}, height = 75 nm, and length = 75 nm.

The apparent permeability K_{app} as a function of p_{out}, D_s, and H is shown in Fig. 9, where K_{abs} is the absolute permeability. As expected, K_{app} continually decreases as D_s decreases to 10^{-8} m^2/s, while K_{app} will not experience any remarkable change when $D_s \leq 10^{-8}$ m^2/s. This is due to the fact that surface diffusivity D_s is small enough that surface diffusion can be neglected compared with micro-scale effects. The same trend is also seen for the relationship of K_{app} vs. p_{out}, where K_{app} shows a marked decrease as p_{out} increases to 30 MPa, while it decreases slowly at $p_{out} = 40$ MPa for the model of large size due to the smaller Kn and smaller $\boldsymbol{u}_g$. At the same value of D_s, the smaller H and p_{out} lead to the larger Kn and larger velocity-slip $\boldsymbol{u}_g$, thereby resulting in a larger K_{app}. There exists a critical case where $Kn \leq 0.001$, then $\boldsymbol{u}_g$ approaches to zero. On this condition, $\boldsymbol{u}_s$ is only influenced by diffusion, rather than micro-scale effect. These results are consistent with those of Wang *et al.*,[40] who simulated the multi-mechanism flow (micro-scale flow and surface diffusion) in long microchannels of different sizes in a wide range of parameters.

Figure 10 shows the relationship between the K_{app} and b, D_s, and H. The K_{app} shows a steady increase as b increases at high values of D_s. At low surface diffusivity (e.g.,

$D_s \leq 10^{-6}$ m^2/s), it shows a downward trend with the increase of b when $H \leq 100$ nm, while it presents an opposite trend for the large-size model (e.g., $H = 300$ nm). This is because the larger the b, the larger the θ. For the case with a smaller-size model, the local Knudsen number is larger, which leads to a larger $\boldsymbol{u}_g$, and then the micro-scale effects become dominant compared with the surface diffusion on this condition, so K_{app} decreases as b increases when $H \leq 100$ nm. Additionally, this similar factor is also responsible for the opposite trend for the large-size model. These tendencies were also verified by Wang *et al.*'s results,[40] which showed that the relationship of K_{app} vs. b was determined by both micro-gaseous flow and surface diffusion. The effects of b, q_{sat}, and H on K_{app} also show a similar pattern as depicted in Fig. 11.

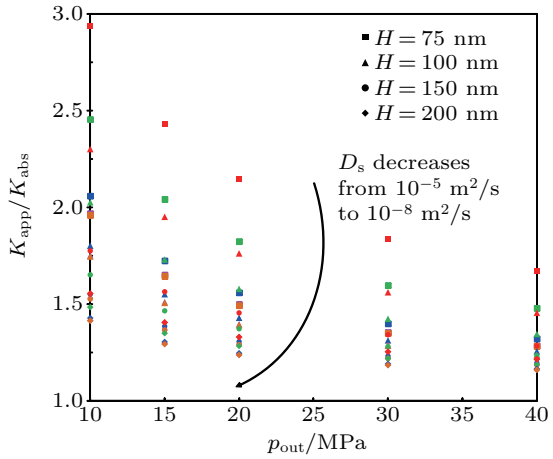


Fig. 9. Relationship between normalized apparent permeability and outlet pressure p_{out} for different values of model size H and surface diffusivity D_s: $D_s = 10^{-8}$ m^2/s (brown), 10^{-7} m^2/s (purple), 10^{-6} m^2/s (blue), 5×10^{-6} m^2/s (green), 10^{-5}m^2/s (red). Other parameters are $\nabla p = 0.1$ MPa/m, $q_{sat} = 4000$ mol/m^3, and $b = 0.125$ MPa^{-1}.

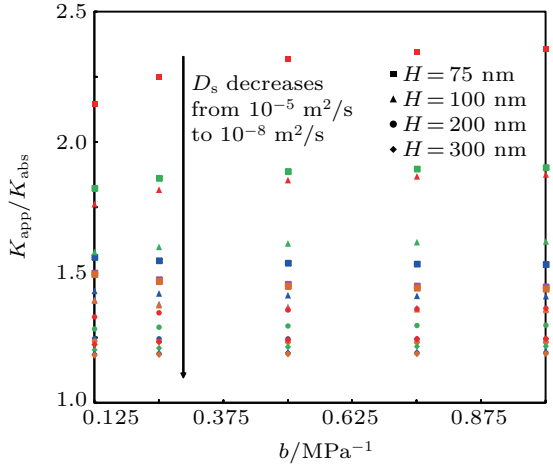


Fig. 10. Relationship between the normalized apparent permeability and Langmuir constant b for different values of model size H and surface diffusivity D_s: $D_s = 10^{-8}$ m^2/s (brown), 10^{-7} m^2/s (purple), 10^{-6} m^2/s (blue), 5×10^{-6} m^2/s (green), 10^{-5} m^2/s (red). Other parameters are $\nabla p = 0.1$ MPa/m, $p_{out} = 20$ MPa, and $q_{sat} = 4000$ mol/m^3.

In this section, the tree-like model composed of straight channels and inclined channels is employed to represent the shale matrix as done in previous studies.[53,72] Our validations above have carefully verified the present scheme, and it can be directly extended to addressing the tree-like model, which was evinced by previous studies.[18,32,42] Moreover, to some extent, our results are in agreement with Wang *et al.*'s results.[40] Therefore, the present model can effectively simulate multi-mechanism flow in the tree-like model.

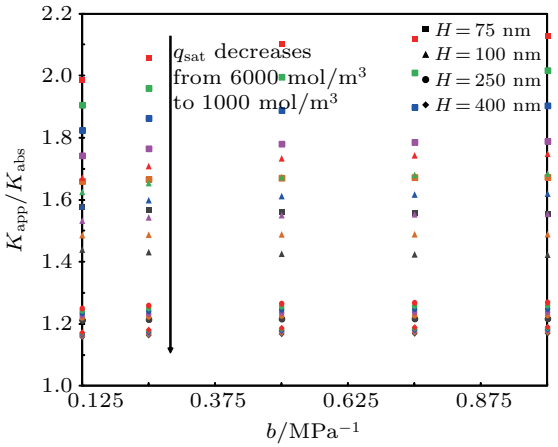


Fig. 11. Relationship between normalized apparent permeability and Langmuir constant b for different values of model size H and Langmuir volume q_{sat}: $q_{sat} = 1000$ mol/m^3 (gray), 2000 mol/m^3 (brown), 3000 mol/m^3 (purple), 4000 mol/m^3 (blue), 5000 mol/m^3 (green), 6000 mol/m^3 (red). Other parameters are $\nabla p = 0.1$ MPa/m, $p_{out} = 20$ MPa, and $D_s = 10^{-6}$ m^2/s.

4. Conclusions

Methane gas flow in organic-rich pores involves the coupling effect of multi-scale and multi-mechanism flow, specifically, the coupling of micro-gaseous flow and surface diffusion caused by methane adsorption/desorption in the pores. In this study, an LBM-based boundary scheme, which combines the non-equilibrium extrapolation scheme and half-way DBB scheme, is proposed to address this coupling effect by incorporating the Langmuir slip boundary into the single-relaxation-time lattice Boltzmann method. Several conclusions can be drawn as follows.

1) An algorithm for thinning digital patterns is employed to obtain the skeleton of pore structures, through which the local Knudsen number for a fluid node and local pressure gradient along skeleton line are calculated for better capturing micro-gaseous flow and surface diffusion along irregular organic-rich pores. By considering viscosity correction and regularization procedure, the present model can effectively resolve the high Knudsen number gas flows. Additionally, a subiteration strategy is proposed to address the coupling effect of micro-gaseous flow and surface diffusion.

2) The present scheme can effectively capture the coupling effect of micro-gaseous flow and surface diffusion in organic pores. An analytical solution under some assumptions is derived to further validate the present model, and good agreement is observed between our numerical results and analytical

solutions. In addition, it achieves a higher accuracy than the existing studies, and also has the potential in modeling multi-scale and multi-mechanism flow in irregular pores. This study has extended it to simulate the multi-mechanism flow in a tree-like porous medium. Its effectiveness and accuracy are verified by the benchmarking cases and the comparisons with the existing results.

3) Multi-mechanism flow in the tree-like model is also numerically investigated and analyzed in a wide range of parameters. Our predicted results are consistent with Wang *et al.*'s results,[40] indicating that the present model is capable of modeling the multi-mechanism flow in irregular micro/nanoscale pores.

Our future work aims at extending the application of the present scheme to the complicated porous media and three-dimensional (3D) cases with GPU (CUDA C) platform.

References

[1] Landry C J, Prodanović M and Eichhubl P 2016 *Int. J. Coal Geology* **159** 120
[2] Zuo H, Deng S, Huang Z, Xiao C, Zeng Y and Jiang J 2018 *Int. J. Oil, Gas and Coal Technology*
[3] Yin Y, Qu Z G and Zhang J F 2017 *Fuel* **210** 569
[4] Wu K, Li X, Guo C, Wang C and Chen Z 2016 *Spe Journal.* **21** 1
[5] Kazemi M and Takbiri-Borujeni A 2015 *Int. J. Coal Geology* **146** 188
[6] Cui X, Bustin A M M and Bustin R M 2009 *Geofluids* **9** 208
[7] Hannon M J and Finsterle S 2017 *Transp. Porous Media.* **123** 545
[8] Liu H, Dan G and Chen J 2018 *Petroleum Science* **15** 116
[9] Sander R, Pan Z and Connell L D 2017 *J. Nat. Gas Sci. & Eng.* **37** 248
[10] Zhao J, Yao J, Zhang L, Sui H and Zhang M 2016 *Int. J. Heat & Mass Transfer* **103** 1098
[11] Yu H, Chen J, Zhu Y B, Wang F C and Wu H A 2017 *Int. J. Heat & Mass Transfer* **111** 1172
[12] Xue Q, Tao Y, Liu Z, Lu S, Li X, Wu T, Jin Y and Liu X 2015 *Rsc Adv.* **5** 25684
[13] Lin K, Yuan Q and Zhao Y P 2017 *Comput. Mater. Sci.* **133** 99
[14] Christou C and Dadzie S K 2016 *Spe Journal.* **21** 938
[15] Geng L, Li G, Zitha P, Tian S, Sheng M and Fan X 2016 *Fuel* **181** 887
[16] Qian Y H, D'Humières D and Lallemand P 1992 *Epl* **17** 479
[17] Shan X, Yuan X and Chen H 2006 *J. Fluid Mech.* **550** 413
[18] Guo Z and Shu C 2013 *Lattice Boltzmann Method and its Applications in Engineering* (Singapore: World Scientific Publishing Co. Pte. Ltd)
[19] Succi S 2001 *The Lattice Boltzmann Equation for Fluid Dynamics and Beyond* (New York: Clarendon Press)
[20] Guo Z and Zheng C 2008 *Int. J. Comput. Fluid Dyn.* **22** 465
[21] Guo Z, Zheng C and Shi B 2008 *Phys. Rev. E* **77** 036707
[22] Guo Z L, Shi B C and Zheng C G 2007 *Epl* **80** 24001
[23] Tang G H, Zhang Y H, Gu X J and Emerson D R 2008 *Epl* **83** 226
[24] Zhang Y H, Gu X J, Barber R W and Emerson D R 2006 *Phys. Rev. E* **74** 046704
[25] Chikatamarla S S and Karlin I V 2009 *Phys. Rev. E* **79** 046701
[26] Chikatamarla S S and Karlin I V 2006 *Phys. Rev. Lett.* **97** 190601
[27] De I L, Rouet J L and Izrar B 2011 *Phys. Rev. E* **84** 066705
[28] Dehdashti E 2016 *Chin. Phys. B* **25** 024702
[29] Zuo W, Yan L and Jia-Zhong Z 2016 *Acta Phys. Sin.* **65** 291 (in Chinese)
[30] Guo Z, Shi B and Zheng C 2011 *Computers & Mathematics with Applications* **61** 3519
[31] Chai Z, Guo Z, Zheng L and Shi B 2008 *J. Appl. Phys.* **104** 014902
[32] Chai Z, Shi B, Guo Z and Lu J 2010 *Commun. Comput. Phys.* **8** 1052
[33] Tao S and Z G 2015 *Phys. Rev. E* **91** 043305
[34] Luo L S 2009 *J. Comput. Phys.* **228** 147
[35] Ansumali S and Karlin I V 2002 *Phys. Rev. E* **66** 026311
[36] Zhao J, Yao J, Li A, Zhang M, Zhang L, Yang Y and Sun H 2016 *J. Appl. Phys.* **120** 579
[37] Tao S and Guo Z 2017 *Chem. Eng. & Technol.* **40** 1758
[38] Tao S, Zhang H and Guo Z 2017 *J. Aerosol Sci.* **103** 105
[39] Fathi E and Akkutlu I Y 2012 *Spe J.* **18** 27
[40] Wang J, Kang Q, Chen L and Rahman S S 2017 *Int. J. Coal Geology* **169** 62
[41] Wang L, Zeng Z, Zhang L, Qiao L, Zhang Y and Lu Y 2018 *Physica A* **495** 180
[42] Guo Z, Zheng C and Shi B 2002 *Phys. Fluids* **14** 2007
[43] Inamuro T, Yoshino M and Ogino F 1995 *Phys. Fluids* **7** 2928
[44] Ning Y, Jiang Y, Liu H and Qin G 2015 *J. Nat. Gas Sci. & Eng.* **26** 345
[45] Chen Y Y, Yi H H and Li H B 2008 *Chin. Phys. Lett.* **25** 184
[46] Chen L, Fang W, Kang Q, De'Haven H J, Viswanathan H S and Tao W Q 2015 *Phys. Rev. E* **91** 033004
[47] Chen L, Kang Q, Dai Z, Viswanathan H S and Tao W 2015 *Fuel* **160** 346
[48] Wang J, Chen L, Kang Q and Rahman S S 2016 *Fuel* **181** 478
[49] Tan Y L, Teng G R and Ze Z 2010 *Chin. Phys. Lett.* **27** 174
[50] Ren J, Guo P, Guo Z and Wang Z 2015 *Transp. Porous Media* **106** 285
[51] Ren J, Guo P, Peng S and Yang C 2016 *J. Nat. Gas Sci. & Eng.* **29** 7
[52] Ren J 2015 *Study of Microscopic Transport Mechanisms of Shale Gas Using the Lattice Boltzmann method* (Chengdu: Southwest Petroleum University)
[53] Ren J, Guo P, Peng S and Yang C 2016 *J. Nat. Gas Sci. & Eng.* **29** 169
[54] Myong R S 2004 *J. Comput. Phys.* **195** 655
[55] Bhattacharya D K and Eu B C 1987 *Phys. Rev. A* **35** 821
[56] Wang J, Li C, Kang Q and Rahman S S 2016 *Int. J. Heat & Mass Transfer* **95** 94
[57] Succi S 2002 *Phys. Rev. Lett.* **89** 064502
[58] Guo Z S 2013 *Lattice Boltzmann Method and its Applications in Engineering*
[59] Zhang R, Shan X and Chen H 2006 *Phys. Rev. E* **74** 046703
[60] Suga K 2013 *Fluid Dyn. Res.* **45** 034501
[61] Latt J and Chopard B 2006 *Math. & Comput. Simul.* **72** 165
[62] Zhang T Y and Suen C Y 1984 *Communications of the ACM* **27** 236
[63] Silin D and Patzek T 2006 *Phys. A* **371** 336
[64] Ohwada T, Sone Y and Aoki K 1989 *Phys. Fluids A Fluid Dyn.* **1** 1588
[65] Li Q, He Y L and Tao W Q 2011 *Microfluid. & Nanofluid.* **10** 607
[66] Shen C, Tian D B, Xie C and Fan J 2004 *Microscale Thermophysical Eng.* **8** 423
[67] Lee T and Lin C L 2005 *Phys. Rev. E* **71** 046706
[68] M Aminpour S G T, Scheuermann A and Li L 2018 *Phys. Rev. E* **98** 043110
[69] Pan C, Luo L S and Miller C T 2006 *Comput. & Fluids* **35** 898
[70] He X, Zou Q, Luo L S and Dembo M 1997 *J. Stat. Phys.* **87** 115
[71] Mousavi M A 2012 *Transp. Porous Media* **94** 537
[72] Sakhaee-Pour A and Bryant S L 2014 *Aapg Bull.* **98** 663
[73] Zou Q and He X 1997 *Phys. Fluids* **9** 1591
[74] Ambrose R J, Hartman R C, Diaz-Campos M, Akkutlu I Y and Sondergeld C H 2012 *Spe J.* **17** 219
[75] Hadjiconstantinou N G 2003 *Phys. Fluids* **15** 2352